Integrated SnO₂ nanorod array with polypyrrole coverage for high-rate and long-life lithium batteries†

Lei Zhang,‡ Kangning Zhao,‡ Wangwang Xu,‡ Yifan Dong, Rui Xia, Fengning Liu, Liang He,* Qiulong Wei, Mengyu Yan and Liqiang Mai*

Conversion/alloying reactions, in which more lithium ions are involved, are severely handicapped by the dramatic volume changes. A facile and versatile strategy has been developed for integrating the SnO₂ nanorod array in the PPy nanofilm for providing a flexible confinement for anchoring each nanorod and maintaining the entire structural integrity and providing sustainable contact; therefore, exhibiting much more stable cycling stability (701 mA h g^{-1} after 300 cycles) and better high-rate capability (512 mA h g^{-1} at 3 A g^{-1}) when compared with the core–shell SnO₂–PPy NA.

Introduction

Concerns over limited energy resources, as well as the need to decrease greenhouse gas emissions, have stimulated the demands to apply renewable energy resources at a large scale, along with the widespread application of hybrid and electric vehicles.[1–4] Among the various energy conversion/storage systems proposed, lithium ion battery is very well positioned to satisfy these needs, but research towards high capacity and high rate capability is still imperious.[5–10] Progress in the study of insertion compounds enabled the development and commercialisation of lithium ion batteries, but a paradigmatic shift in energy density will only be achieved with the use of electrodes operating through alternative reaction mechanisms, namely the conversion reaction and the alloy reaction, allowing for more electrons per atom utilized, which are associated with much higher energy densities than that of insertion reactions.[11–16]

Among them, SnO₂ attracts particular attention due to its high theoretical capacity and safe working potential.[17–25] The high theoretical capacity originates from the two-step reaction that SnO₂ generally is regarded to witness:[26]

$$SnO_2 + 4Li^+ + 4e^- = Sn + 2Li_2O$$

$$Sn + 4.4Li^+ + 4.4e^- = Li_{4.4}Sn$$
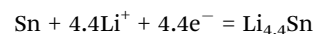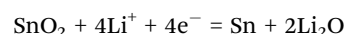
The initial process is a conversion reaction, yielding tin particles and Li₂O, which is generally regarded as irreversible.[27] The following alloying process is widely known to be reversible and 4.4 mol lithium ions can be reversibly alloyed and dealloyed with Sn, resulting in a large volume expansion–contraction ($\sim$300%).[28] The huge variation in volume is generally regarded as the result of severe capacity fading. Due to the above-mentioned two-step reaction, more lithium ions are induced into the host structure, bringing about higher volume expansion upon cycling, leading to the disintegration and pulverization of the electrode, resulting in the continuous breakdown and frequent formation of a very thick solid electrolyte interphase (SEI) and consumption of the electrolyte.[29] Therefore, a rational design should take all of the abovementioned considerations into account to improve the cycle performance of SnO₂.

Core–shell structure through conformal coatings with amorphous carbon and metallic coatings has been demonstrated as an efficient strategy to improve the excellent electrochemical performance.[30–40] However, upon the volume expansion of the electrode, especially for the large-volume-variation electrodes, these coatings will fracture, leading to the loss of contact and the surface of the active materials will still be exposed to electrolyte. Thus, more robust protection through coating for
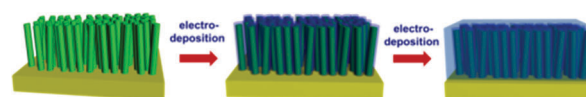
State Key Laboratory of Advanced Technology for Materials Synthesis and Processing, Wuhan University of Technology, Wuhan 430070, China.
E-mail: mlq518@whut.edu.cn, hel@whut.edu.cn

† Electronic supplementary information (ESI) available. See DOI: 10.1039/c5cp00150a
‡ These authors contributed equally to this study.

Fig. 1 Schematic illustration of the formation process of the SnO₂–PPy nanofilm.

This journal is © the Owner Societies 2015

Phys. Chem. Chem. Phys., 2015, **17**, 7619–7623 | 7619

stress relieving is urgently needed to be designed for more stable SEI layer in achieving long-cycle life.[41–48]

Herein, to design robust protection for large-volume-change materials, we rationally proposed a facile strategy for the fabrication of SnO_2–PPy nanofilm through hydrothermal treatment followed by subsequent electrodeposition. Unlike the core–shell structure, this type of a unique structure is able to possess the property of integrating SnO_2 nanorod under the PPy film coverage entirely, and thus ensuring steady and continuous contact between the PPy and SnO_2 nanorod array as well as the substrate, promising good cycling stability as anode for lithium battery (Fig. 1). Our strategy is to design an optimized electrode with more flexible protective shell and more sustainable core–shell contact, yielding strain-relaxation and continuous electric contact simultaneously, with low weight percentage against active material.

Experimental

Synthesis of the bare SnO_2 nanorod arrays

The synthesis processes were the same as the one reported previously.[46] In a typical experiment, $SnCl_4 \cdot 5H_2O$ (0.73 g) and NaOH (1.25 g) were dissolved into 30 mL distilled water. After half an hour of magnetic stirring, 50 mg NH_4F was added into the solution. The solution was transferred into a Teflon-lined autoclave (50 mL), in which a piece of cleaned nickel foam substrate was beforehand placed standing against the wall, and heated to 200 °C for 24 h. The nickel foam acted as a substrate for SnO_2 nanorod arrays during the hydrothermal process. The as-deposited bare SnO_2 nanorod arrays were rinsed repeatedly with deionized water and dried at 60 °C for 8 h. The average mass of SnO_2 nanorod array (SnO_2 NA) was 1.67 ± 0.35 mg cm^{-2}, which was calculated by the mass difference of the as-prepared samples before and after the hydrothermal treatment.

Preparation of core–shell SnO_2–PPy NA, SnO_2–PPy nanofilm

Bare SnO_2 nanorod arrays were used as the backbone for the growth of PPy shell. The electrolyte used for electro-polymerization of PPy was 100 mM lithium perchlorate and 10 mM pyrrole monomer in acetonitrile solution. The electro-polymerization of PPy was carried out in a three-compartment system, using the bare SnO_2 nanorod arrays electrode as the working electrode, Ag/AgCl as the reference electrode and Pt foil as the counter electrode. The core–shell SnO_2–PPy nanorod array (core–shell SnO_2–PPy NA) and SnO_2–PPy nanofilm was deposited using a CHI760D electrochemical workstation through a constant current chronopotentiometry method at a current density of 1.6 mA cm^{-2} for 700 s and 2000 s, respectively.

Characterization

The crystallographic information of the obtained products was measured with a Bruke D8 Discover X-ray diffraction (XRD) measurement using Cu Kα radiation in a coupled 2θ mode at room temperature. Field emission scanning electron microscopy (FESEM) images were recorded with a JEOL-7100F.

Energy dispersive X-ray spectra (EDS) were recorded by an Oxford EDS IE250. Fourier transform infrared (FT-IR) transmittance spectra were recorded using the 60-SXB IR spectrometer. The electrochemical performance was characterized with the coin cells of CR2016 type assembled in a glove-box filled with pure argon gas. Lithium foil was used as the anode, a solution of $LiPF_6$ (1 M) in EC/DEC (1 : 1 vol/vol) was used as the electrolyte, and the as-prepared samples as the cathode. Galvanostatic charge/ discharge measurement was performed with a multichannel battery testing system (LANDCT2001A), cyclic voltammetry (CV) and electrochemical impedance spectroscopy (EIS) were measured by an Autolab Potentiostat Galvanostat at room temperature. Brunauer–Emmett–Teller (BET) surface areas were measured using a Tristar II 3020 instrument to measure the adsorption of nitrogen.

Details of finite element model simulation

The finite element model (FEM) simulation of the micro-mechanical behaviours of the free-standing SnO_2 NA, core–shell SnO_2–PPy and SnO_2–PPy film was carried out using an ANSYS workbench to predict and identify the displacement/ deformation of these nanostructures. In the simulation the density, Young's modulus and Poisson ratio of the SnO_2 nanorod was set as 6.95 g cm^{-3}, 37.2 GPa and 0.21, respectively, and the density, Young's modulus and Poisson ratio of the PPy films was set as 0.97 g cm^{-3}, 3.6 GPa cm^{-3}, and 0.21, respectively. Free quad mesh was defined in all the models. In our simulations, an isotropic initial stress of 0.1 MPa was applied in the domain of the nanorod to simulate the diffusion-induced stress, resulting from the ion intercalating. The diameter of the nanorod was 100 nm.

Results and discussion

Initially, XRD analysis was carried out to investigate the crystal structure (Fig. 2A). All the diffraction peaks of the bare SnO_2 NA, core–shell SnO_2–PPy NA and SnO_2–PPy nanofilm is well indexed to the tetragonal rutile structure of SnO_2 (JCPDS No. 41-1445). Four well-defined identified diffraction peaks at 26.5°, 33.8°, 37.81° and 51.81° can be well assigned to (110), (101), (200) and (211) planes of tetragonal SnO_2, respectively.
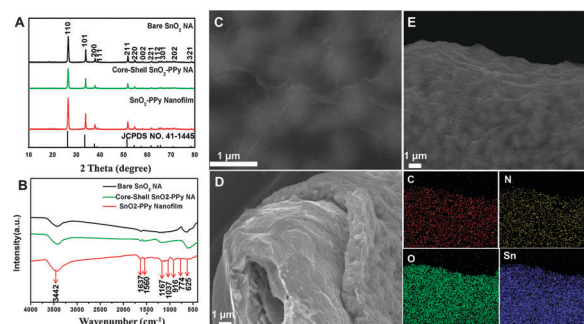

Fig. 2 (A) XRD patterns of bare SnO_2 NA, core–shell SnO_2–PPy NA, and SnO_2–PPy nanofilm; (B) FT-IR spectra of the bare SnO_2 NA, and SnO_2–PPy nanofilm; (C, D) SEM images of SnO_2–PPy nanofilm; (E) EDS element mappings of C, N, O and Sn, respectively.

Moreover, there were no evident differences among the three samples, indicating that the electrodeposition process had no influence on the tin oxide array and no other peaks were observed for PPy. Thus, to further identify the existence of PPy, FT-IR test was carried out to test the bare SnO_2 NA and SnO_2–PPy nanofilm (Fig. 2B). In these spectra, the bands in the range of 537–623 cm^{-1} were observed for both bare SnO_2 NA and SnO_2–PPy nanofilm can be assigned to the anti-symmetric and symmetric vibrations of Sn–O–Sn. The bands centred at 1637 and 1560 cm^{-1} for both the SnO_2–PPy nanofilm and the PPy correspond to the typical C=C in plane vibration. In addition, the characteristic bands of deformation vibrations of the C–N stretching vibration of polypyrrole skeleton were found at 1167 and 1037 cm^{-1}. The band at 916 cm^{-1} is assigned to C–H vibrations. Thus, these characteristic bands of PPy for both SnO_2–PPy nanofilm and PPy were nearly identical, except for the lower intensity observed with lower PPy content in the SnO_2–PPy nanofilm. The FT-IR results provided direct evidence that PPy was present in the SnO_2–PPy nanofilm. Furthermore, the morphologies of the as-prepared samples were characterized by SEM. The SnO_2 nanorods were initially captured by the small PPy nanosheet at each side of the nanorod uniformly, forming core–shell SnO_2–PPy NA. Moreover, with increased deposition time, the PPy nanosheets grown on each SnO_2 nanorod interconnected, forming the SnO_2–PPy nanofilm. Moreover, the thickness of the SnO_2–PPy nanofilm was around 1 μm (Fig. 2D). To further estimate the existence of PPy in SnO_2–PPy nanofilm, the EDS elemental mapping was carried out. As can be observed in Fig. 2E, Sn, C, N, and O were uniformly distributed in the range of the image, indicating the even coating of PPy, which was also confirmed by the semiquantitative EDAX results. Moreover, the mass of PPy calculated by the mass difference of the as-prepared samples before and after electrodeposition after drying at 70 °C for 24 h was 0.20 ± 0.05 mg cm^{-2}, which was 12% as high as that of the active material SnO_2, indicating the low density of the as-deposited PPy film.

Intrigued by the structural features of SnO_2–PPy nanofilm, coin cells (2016 type) of these samples were assembled by using lithium plate as anode at a voltage range between 0.005 and 2 V to test the electrochemical performance at room temperature. Initially, the cycle performance at current density of 200 mA h g^{-1} was performed (Fig. 3). The initial capacity of the bare SnO_2 NA, core–shell SnO_2–PPy NA, and SnO_2–PPy nanofilm is 1450, 1600, 1738 mA h g^{-1}, respectively, which was mainly contributed by the SnO_2 nanorod array (Fig. S9, ESI†). During cycling, the capacity fluctuated, which results from the temperature variation of the seasonal changes and diurnal temperature difference. Despite this, the SnO_2–PPy nanofilm exhibits the most stable cycling performance producing the 300th capacity of 701 mA h g^{-1}. The initial capacity fading may result from the irreversible reaction of the first process. Of all the three samples, the SnO_2–PPy nanofilm exhibits the most stable cycling stability. From 50 to 300 cycles, the capacity retention of SnO_2–PPy nanofilm was 87.5%, which was much higher than that of core–shell SnO_2–PPy NA (48.9%). The capacity of the bare SnO_2 NA approached lower than 100 mA h g^{-1}, making the definition of the capacity
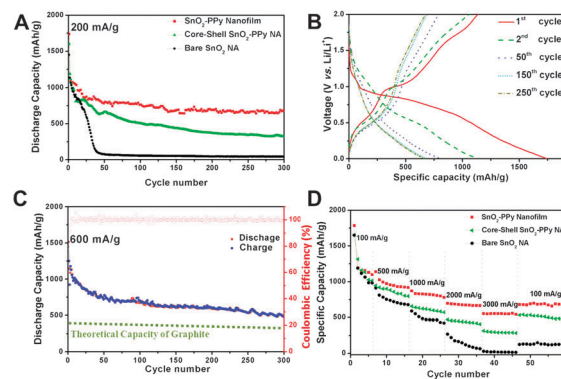

Fig. 3 Electrochemical characteristics: (A) cycle performance of bare SnO_2 NA, core–shell SnO_2–PPy NA, and SnO_2–PPy nanofilm at a current density of 200 mA h g^{-1}; (B) galvanostatic charge–discharge curves of SnO_2–PPy nanofilm at the current density of 200 mA g^{-1}; (C) cycling performance of SnO_2–PPy nanofilm at high current density of 600 mA g^{-1}; (D) rate performance of bare SnO_2 NA, core–shell SnO_2–PPy NA, and SnO_2–PPy nanofilm.

retention insignificant. Further the current density was increased to 600 mA h g^{-1} to identify the high-rate cycling stability. The capacity even after 300 cycles was 500 mA h g^{-1}, which was still well above the theoretical capacity of the graphite (372 mA h g^{-1}). Moreover, the coulombic efficiencies, except for the first cycle, remain around 100%, indicating the stable SEI layer and excellent structural stability without electrolyte continuous decomposition.

Furthermore, the rate performance was investigated at different current densities of 100, 500, 1000, 2000, 3000 and back to 100 mA g^{-1}. As can be seen in Fig. 3D, the discharge capacities of the SnO_2–PPy nanofilm were 1099, 917, 777, 664, 512, and 691 mA h g^{-1}. Noticeably, even at a high current density of 3 A g^{-1}, the capacity was 512 mA h g^{-1}, showing an excellent high-rate capacity. Moreover, the capacity at each current density was far higher than that of the bare SnO_2 NA, core–shell SnO_2–PPy NA. Although suffering from high current density, the SnO_2–PPy nanofilm still retains good capacity and excellent cycling stability.

Initially, in order to further identify that if the PPy nanofilm can act as a thin and robust protection, the SEM images of the bare SnO_2 NA, core–shell SnO_2–PPy NA and SnO_2–PPy nanofilm after 300 cycles are shown in Fig. 4. For the bare SnO_2 NA (Fig. S10, ESI†), the SnO_2 nanorods can hardly be observed; many small pores can be seen on the surface, which can be attributed to the enormous volume variation during cycling. As for the core–shell SnO_2–PPy NA, there are also small amount of active material left on it. However, the nanorod turns out to show a very smooth surface, which may be because the PPy still captured the nanorods steadily, indicating that the contact between core–shell SnO_2–PPy NA and the nickel foam was still lost easily, leading to poor cycling stability. However, unlike the bare SnO_2 NA and core–shell SnO_2–PPy NA, the SEM images of SnO_2–PPy nanofilm turn out to be almost the same with that before cycling. Thus, there turns out to be many pores on the film, which may have resulted from the expansion of the SnO_2 nanorod. In order to further prove that if the SnO_2 nanorods were captured by PPy, EDX mapping was carried out, in which the elements C, N, Sn, and O were distributed
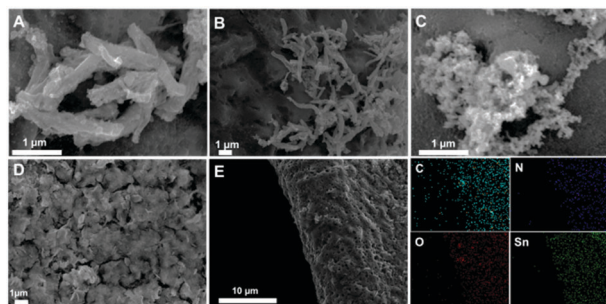
Fig. 4 SEM images of core–shell SnO_2–PPy NA (A, B), SnO_2–PPy nanofilm (C, D) after cycling for 300 cycles at current density of 200 mA h g^{-1}; EDX mapping of SnO_2–PPy nanofilm (E) after cycling for 300 cycles at current density of 200 mA h g^{-1}.

uniformly in the selected area, indicating a good contact between SnO_2–PPy nanofilm and the nickel foam even after long cycles. The particles on the surface may be the electrolyte that got dried during the SEM sample preparation. The EIS spectra of the three different samples were carried out to provide the insight of the kinetic (Fig. S3, ESI†). The EIS spectrum shows two compressed semicircles from the high to medium frequency range of each spectrum, which describes the charge transfer resistance (R_{ct}) for these electrodes, and a line inclined at approximately 45° in the low-frequency range, which could be considered as Warburg impedance (Z_W) and has been fitted in this circuit, in which R_1 represents the Ohmic resistance of the electrode system, including the electrolyte and the cell components. R_2 and R_3 represent the resistance related to SEI and the charge transfer, respectively. CPE_1, CPE_2 and Z_w are the capacitance related to SEI, double layer impedance and Warburg impedance,[49,50] respectively. The values of R_{ct} for the bare SnO_2 NA, core–shell SnO_2–PPy NA, and SnO_2–PPy nanofilm are 41, 70, and 92 Ω, respectively, suggesting fast kinetic for SnO_2–PPy nanofilm. In additional, the slopes at low-frequency range were almost the same among the three different samples, suggesting that the ion diffusion rate is almost the same. Besides, finite element method simulations were carried out and gave insight in the deformation of the nanorod array in the bare SnO_2 NA, core–shell SnO_2–PPy NA, and SnO_2–PPy nanofilm. The initial stress was applied to simulate the diffusion-induced stress, resulting from the ion intercalation. The migration modulus was calculated and plotted in each model and presented in Fig. 5. The SnO_2 nanorod in the bare SnO_2 NA, core–shell SnO_2–PPy NA witnessed severe deformation and by integrating the conducting polymer coverage entirely, SnO_2 nanorods in SnO_2–PPy nanofilm witnessed the least deformation, indicating the most anti-pulverization property.

Based on the abovementioned results, the SnO_2–PPy nanofilm exhibits outstanding cycling stability and high rate capability
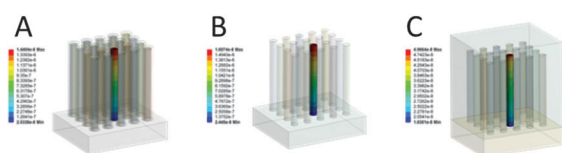
when compared with bare SnO_2 NA and core–shell SnO_2–PPy NA. This can be attributed to the unique structure, confining the SnO_2 nanorod array in the PPy coverage. Initially, integrating the conducting polymer coverage provides a flexible confinement for anchoring each nanorod and maintaining the entire structural integrity and providing sustainable contact. Upon charging and discharging, the flexible conducting polymer PPy film can effectively act as a 'buffering agent' for accommodating severe stress resulting from the volume expansion of SnO_2 nanorod, and avoid the aggregation of tin oxide nanorods. Besides, the thick PPy film is assembled by small nanosheets with pores, which will not influence the contact between the active materials and the electrolyte, leading to fast lithium ion diffusion rate and effectively reducing the degree of the repeated formation/decomposition of SEI film. In addition, both the conducting polymer and the nick foam together provide continuous electron transport for the entire structure and more free space for fast charge and mass transfer, resulting in enhanced rate capability.

Conclusions

A facile and versatile strategy has been developed for fabricating the SnO_2–PPy nanofilm. When evaluated as anode for lithium battery, the SnO_2–PPy nanofilm exhibits a capacity retention of 87.5% from 50 to 300 cycles, which is much higher than that of core–shell SnO_2–PPy NA (48.9%), showing outstanding cycling stability and high-rate capability compared with the electrode of bare SnO_2 NA, core–shell SnO_2–PPy NA. The enhanced performance is attributed to the reason that the conducting polymer provides a flexible confinement for anchoring each nanorod and maintaining the entire structural integrity and offers 'buffering' for accommodating and more free space for charge and mass transfer. An exploration and development of the multifunctional composite with conductive polymer have been developed, realizing the benefits to fabricate new composite anodes with desired capacity, high-rate capability, and cycling stability. More significantly, this flexible PPy film holds the potential in severing as stretchy shell for conversion or alloying-based electrode materials or even being used in other fields, such as material protection, bionic design and drug delivery.

Conflicts of interest

All authors discussed the results and commented on the manuscript. The authors declared no competing financial interest.

Acknowledgements

Fig. 5 The calculated deformation contour for the bare SnO_2 NA (A), core–shell SnO_2–PPy NA (B), and SnO_2–PPy nanofilm (C).

7622 | *Phys. Chem. Chem. Phys.*, 2015, **17**, 7619–7623

This journal is © the Owner Societies 2015

Notes and references

1 P. G. Bruce, S. A. Freunberger, L. J. Hardwick and J.-M. Tarascon, *Nat. Mater.*, 2011, **11**, 19–29.
2 Y. M. Chiang, *Science*, 2010, **330**, 1485–1486.
3 D. Larcher and J. M. Tarascon, *Nat. Chem.*, 2015, **7**, 19–29.
4 K. Xu, *Chem. Rev.*, 2014, **114**, 11503–11618.
5 M. N. Obrovac and V. L. Chevrier, *Chem. Rev.*, 2014, **114**, 11444–11502.
6 D. Butler, *Nature*, 2007, **445**, 586–588.
7 S. Chu and A. Majumdar, *Nature*, 2012, **488**, 294–303.
8 D. Lindley, *Nature*, 2010, **463**, 18–20.
9 Z. Peng, S. A. Freunberger, Y. Chen and P. G. Bruce, *Science*, 2012, **337**, 563–566.
10 P. Simon, Y. Gogotsi and B. Dunn, *Science*, 2014, **343**, 1210–1211.
11 P. L. Taberna, S. Mitra, P. Poizot, P. Simon and J. M. Tarascon, *Nat. Mater.*, 2006, **5**, 567–573.
12 A. Magasinski, P. Dixon, B. Hertzberg, A. Kvit, J. Ayala and G. Yushin, *Nat. Mater.*, 2010, **9**, 353–358.
13 A. R. Armstrong, C. Lyness, P. M. Panchmatia, M. S. Islam and P. G. Bruce, *Nat. Mater.*, 2011, **10**, 223–229.
14 N. Liu, H. Wu, M. T. McDowell, Y. Yao, C. Wang and Y. Cui, *Nano Lett.*, 2012, **12**, 3315–3321.
15 P. Senguttuvan, G. Rousse, H. Vezin, J. M. Tarascon and M. R. Palacín, *Chem. Mater.*, 2013, **25**, 2391–2393.
16 C. Wang, H. Wu, Z. Chen, M. T. McDowell, Y. Cui and Z. Bao, *Nat. Chem.*, 2013, **5**, 1042–1048.
17 L. Mai, Q. Wei, Q. An, X. Tian, Y. Zhao, X. Xu, L. Xu, L. Chang and Q. Zhang, *Adv. Mater.*, 2013, **25**, 2969–2973.
18 L. Mai, X. Tian, X. Xu, L. Chang and L. Xu, *Chem. Rev.*, 2014, **114**, 11828–11862.
19 L. Zhang, H. B. Wu, B. Liu and X. W. Lou, *Energy Environ. Sci.*, 2014, **7**, 1013.
20 Y. Zhang, Y. Li, Z. Wang and K. Zhao, *Nano Lett.*, 2014, **14**, 7161–7170.
21 N. Liu, H. Wu, M. T. McDowell, Y. Yao, C. Wang and Y. Cui, *Nano Lett.*, 2012, **12**, 3315–3321.
22 Y. Zhao, J. Feng, X. Liu, F. Wang, L. Wang, C. Shi, L. Huang, X. Feng, X. Chen, L. Xu, M. Yan, Q. Zhang, X. Bai, H. Wu and L. Mai, *Nat. Commun.*, 2014, **5**, 4565.
23 J. Liang, X. Y. Yu, H. Zhou, H. B. Wu, S. Ding and X. W. Lou, *Angew. Chem.*, 2014, **53**, 12803–12807.
24 Y. Liu, N. Zhang, L. Jiao, Z. Tao and J. Chen, *Adv. Funct. Mater.*, 2014, **25**, 214–220.
25 K. Deng, H. Lu, Z. Shi, Q. Liu and L. Li, *ACS Appl. Mater. Interfaces*, 2013, **5**, 7845–7851.
26 H. Tavassol, M. W. Cason, R. G. Nuzzo and A. A. Gewirth, *Adv. Energy Mater.*, 2015, **5**, 1400317.
27 G. A. Elia, J. Wang, D. Bresser, J. Li, B. Scrosati, S. Passerini and J. Hassoun, *ACS Appl. Mater. Interfaces*, 2014, **6**, 12956–12961.
28 Q. Li, P. Wang, Q. Feng, M. Mao, J. Liu, S. X. Mao and H. Wang, *Chem. Mater.*, 2014, **26**, 4102–4108.
29 X. Zhou, Z. Dai, S. Liu, J. Bao and Y. G. Guo, *Adv. Mater.*, 2014, **29**, 3943–3949.
30 W. Chen, L. Qie, Y. Shen, Y. Sun, L. Yuan, X. Hu, W. Zhang and Y. Huang, *Nano Energy*, 2013, **2**(3), 412–418.
31 C. Guan, X. Wang, Q. Zhang, Z. Fan, H. Zhang and H. J. Fan, *Nano Lett.*, 2014, **14**, 4852–4858.
32 J. Qin, C. He, N. Zhao, Z. Wang, C. Shi, E.-Z. Liu and J. Li, *ACS Nano*, 2014, **8**, 1728–1738.
33 X. Zhou, Z. Dai, S. Liu, J. Bao and Y. G. Guo, *Adv. Mater.*, 2014, **26**, 3943–3949.
34 M. Yan, F. Wang, C. Han, X. Ma, X. Xu, Q. An, L. Xu, C. Niu, Y. Zhao, X. Tian, P. Hu, H. Wu and L. Mai, *J. Am. Chem. Soc.*, 2013, **135**, 18176–18182.
35 Y. Yao, N. Liu, M. T. McDowell, M. Pasta and Y. Cui, *Energy Environ. Sci.*, 2012, **5**, 7927–7930.
36 X. Fan, J. Shao, X. Xiao, X. Wang, S. Li, H. Ge and L. Chen, *Nano Energy*, 2014, **9**, 196–203.
37 Q. An, F. Lv, Q. Liu, C. Han, K. Zhao, J. Sheng, Q. Wei, M. Yan and L. Mai, *Nano Lett.*, 2014, **14**, 6250–6256.
38 D. Wang, Y. Zhao, X. Xu, K. M. Hercule, M. Yan, Q. An, X. Tian, J. Xu, L. Qu and L. Mai, *Nanoscale*, 2014, **6**, 8124–8129.
39 Y. Dong, S. Li, H. Xu, M. Yan, X. Xu, X. Tian, Q. Liu and L. Mai, *Phys. Chem. Chem. Phys.*, 2013, **15**, 17165–17170.
40 L. Zhang, K. Zhao, W. Xu, J. Meng, L. He, Q. An, X. Xu, Y. Luo, T. Zhao and L. Mai, *RSC Adv.*, 2014, **4**, 33332.
41 Y. Chen, S. Zeng, J. Qian, Y. Wang, Y. Cao, H. Yang and X. Ai, *ACS Appl. Mater. Interfaces*, 2014, **6**, 3508–3512.
42 D. Chao, X. Xia, J. Liu, Z. Fan, C. F. Ng, J. Lin, H. Zhang, Z. X. Shen and H. J. Fan, *Adv. Mater.*, 2014, **26**, 5794–5800.
43 Y. W. Cheng, C. K. Lin, Y. C. Chu, A. Abouimrane, Z. Chen, Y. Ren, C. P. Liu, Y. Tzeng and O. Auciello, *Adv. Mater.*, 2014, **26**, 3724–3729.
44 Y. L. Ding, Y. Wen, P. A. van Aken, J. Maier and Y. Yu, *Small*, 2014, DOI: 10.1002/smll.201402502.
45 F. H. Du, B. Li, W. Fu, Y. J. Xiong, K. X. Wang and J. S. Chen, *Adv. Mater.*, 2014, **26**, 6145–6150.
46 W. Xu, K. Zhao, C. Niu, L. Zhang, Z. Cai, C. Han, L. He, T. Shen, M. Yan, L. Qu and L. Mai, *Nano Energy*, 2014, **8**, 196–204.
47 H. Zhao, Z. Wang, P. Lu, M. Jiang, F. Shi, X. Song, Z. Zheng, X. Zhou, Y. Fu, G. Abdelbast, X. Xiao, Z. Liu, V. S. Battaglia, K. Zaghib and G. Liu, *Nano Lett.*, 2014, **14**, 6704–6710.
48 R. Raccichini, A. Varzi, S. Passerini and B. Scrosati, *Nat. Mater.*, 2015, **14**, 271–279.
49 A. Birrozzi, R. Raccichinib, F. Nobilia, M. Marinaro, R. Tossici and R. Marassi, *Electrochim. Acta*, 2014, **10**, 228–233.
50 R. Ravikumar and S. Gopukumar, *Phys. Chem. Chem. Phys.*, 2013, **15**, 3712–3717.